PAPER

Fine comminution of torrefied wheat straw for energy applications: properties of the powder and energy balances of the production route

Rova-Karine Rajaonarivony,[a] Xavier Rouau,[a] Jean-Michel Commandré,[b]
Charlène Fabre,[a] Jean-Eudes Maigret,[c] Xavier Falourd,[cd] Sophie Le Gall,[cd]
Bruno Piriou,[b] Camille Goudenhooft,[e] Sylvie Durand,[c] Alain Bourmaud,[e]
Johnny Beaugrand[c] and Claire Mayer-Laigle [ID][a]

Lignocellulosic powders have a chemical composition that makes them explosive under certain conditions. In the form of ultrafine particles, they can be directly used as fuel in combustion devices to generate heat and mechanical power without the need to convert them into a liquid form. However, the production of such powder encounters two main challenges that affect engine efficiency: high energy consumption during grinding and poor flowability of the resulting powder. To tackle these challenges, one option is to modify the chemical and physical characteristics of the biomass before grinding. This can be effectively achieved through thermal pretreatment methods such as torrefaction, which alter the chemical structure of lignocellulosic biomass, making it more brittle, modifying its surface properties, and thereby improving its flowability. In this study, we investigated the impact of two torrefaction temperatures (220 °C and 280 °C) on the chemical and physical properties of wheat straw prior to fine milling. Our results indicate that the physical and chemical properties of the wheat straw were not significantly affected at 220 °C, whereas a significant change was observed at 280 °C. In particular, extensive chemical analysis and atomic force measurements show that the modifications of the properties are related to heat-induced degradation of cell wall polymers and an increase in cellulose crystallinity. For the wheat straw torrefied at 280 °C, both the grindability and flowability of the ground powder improved significantly. Meanwhile, the total energy consumption for the transformation remained constant, making the torrefaction process interesting for designing combustible powders.

1 Introduction

Annual cereal harvests produce huge amounts of renewable biomass in the form of non-edible by-products that can be used for the production of bio-energy in place of fossil feedstock. In particular, several studies demonstrated the potential of pulverized lignocellulosic materials for high-power applications such as gasification processes or even directly fuelling combustion engines.[1–3] In this innovative technology, unlike current fuels derived from biomass, the powder is fed directly into the engine with no treatment other than ultra-fine milling.[4] This invention relies on the fact that when used in sufficient quantity and concentration in a confined environment, finely milled biomass undergoes rapid combustion in the form of deflagration.[5] The energy released can be recovered as a mechanical force and used for high-power generation. Previous studies by our team[4,6–8] have demonstrated that an ultrafine lignocellulosic powder, with a median particle size of around 20 μm, is fully compatible with this application[7] but the energy released depends on the physical and chemical properties of the powder. Thus, the production of such powdered fuel is entirely green, provided that the energy required for the milling remains lower than the heating values of the lignocellulosic biomass.

However, obtaining powder of this order of magnitude requires the plant material to be fractionated below the cellular scale (<50 microns) which poses challenges in terms of energy requirement. Indeed, comminution results from fractures which are initiated and propagated mainly through defect zones[9] naturally present in the structure of the plant. These zones are much more numerous at the plant tissue level than at the cellular scale. As a result, subcellular milling of plant materials usually consumes much more energy.

[a]IATE, Université de Monpellier, INRAE, Montpellier Supagro, 34060 Montpellier, France. E-mail: claire.mayer@inrae.fr

[b]BIOWOOEB, Université de Montpellier, INRAE, Montpellier Supagro, 34060 Montpellier, France

[c]INRAE, UR BIA, 44316 Nantes, France

[d]INRAE, BIBS Facility, PROBE Infrastructure, 44316 Nantes, France

[e]Univ. Bretagne Sud, UMR CNRS 6027, IRDL, F-56100 Lorient, France

In addition, obtaining stable energy yields during engine combustion requires regular feeding which, in turn, means that the lignocellulosic powder must exhibit a good flowability. This is not a straightforward task when dealing with a powder of such size, primarily composed of cell fragments and possessing chemical groups that tend to strengthen interparticle cohesive forces.[10]

Among all the lignocellulosic biomasses, straws from cereal crops (such as wheat straw in Europe, rice straw in Asia…) appear to be suitable candidates for such applications, as their production and collection are spread over vast territories, rather than being limited to a few producer countries. However, previous work studying the grindability of various biomasses, including wheat straw[11–15] has shown that such fibrous materials are more difficult to mill than more brittle materials such as pine bark, regardless of the mill used.[14] Milling efficiency and powder quality differ with the dominant mechanical loading stress generated by the milling device. Milling devices that work by impact as the dominant mechanism tend to generate powders with a better flowability and lower potential agglomeration whereas milling devices that work by attrition as the dominant mechanism make better use of milling energy input and thus provide a more cost-effective comminution process.[13,14,16] Combining both modes of mechanical stress, such as in a stirred ball mill (SBM), appears to be the best compromise, especially for fibrous materials such as wheat straw. Nevertheless, for wheat straw, the milling energy required to reach a 20 μm average particle size (1.37 kW h kg^{-1}) still represented $\frac{1}{3}$ of the lower heating value of straw (4.1 kW h kg^{-1}), i.e. the maximum energy that can be expected to be recovered.[14,17,18]

Improving the grindability of wheat straw and enhancing its energy content constitutes a challenge that needs to be overcome in order to improve the cost-effectiveness of powder production and the technical performances of the powders for different end-uses such as combustion or gasification.[19]

Torrefaction, a mild thermal treatment led under non-oxidizing conditions, is known to increase the energy density of the matter by removing oxygen chemical groups.[20] Additionally, partial thermolysis in the bulk of the constituent polymer chains and modifications in cellulose crystallinity have also been reported, resulting in a weakening of the mechanical properties. This, in turn, facilitates the milling process and influences the properties of the resulting powders, such as surface chemistry, shape, and indeed, flowability.[21–24]

While previous studies have emphasized the impact of torrefaction prior to milling at the tissue scale, none, to the best of our knowledge, has explored its effects specifically for milling processes below the cellular level.

In this study, we first investigated the influence of torrefaction on the chemical and mechanical properties of wheat straw at the cellular level in order to determine the optimal operating conditions. In the second part, we examined how these conditions affect the processability of wheat straw and the properties of the resulting powder, taking into account the specifications required for combustion engine applications. Finally, in the last part, we conducted an energy balance analysis comparing the input processing energy costs and the potential heat release of control and torrefied powders, aiming to discuss the viability of these technical processing routes for high-power applications.

2 Materials and methods

Control wheat straw (WS) and torrefied wheat straw (TWS) were prepared according to two different process routes as summarized in Fig. 1. Each processing step is described in further detail below.

2.1 Raw lignocellulosic biomass

Wheat straw (*Triticum aestivum*) was harvested in the south of France (Saint-Gilles, France) and stored dried in 25-kg bales. Moisture content was measured by weight loss after oven-drying for 2 h at 135 °C.[16] The moisture content of the stored wheat straw was 11%.
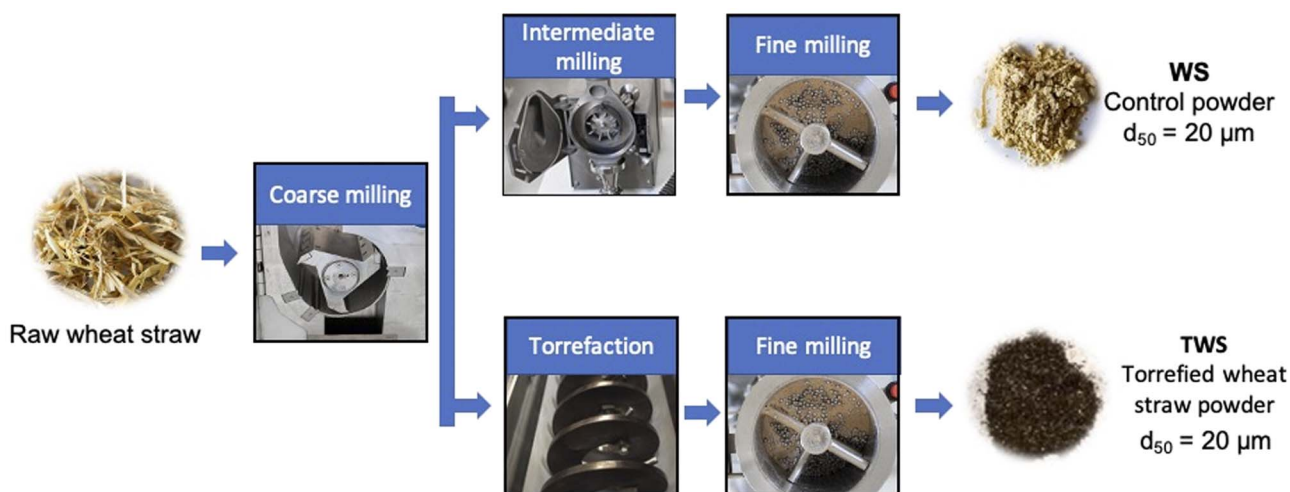

Fig. 1 Technological process routes for the production of control (WS) and torrefied wheat straw (TWS).

2.2 Processing step

Coarse milling of the raw materials: wheat straw (WS) was coarse-milled using a cutting mill (SM 300, Retsch®, Germany) with a 2 mm sieving grid, operated with manual feeding according to protocols previously developed.[14]

2.2.1 Torrefaction of the coarse-milled straw.
The coarse-milled powder of wheat straw was torrefied in a large-scale torrefaction reactor (VT-Green®, Biogreen, Saint-Bonnet-de-Rochefort, France) able to prepare enough material for experiments in pilot-scale mills (about 10 kg h^{-1}).[14,25] The raw material was heated in a nitrogen flow by an electrically heated Spirajoule™-type screw conveyor. The straw sample was torrefied at 220 °C and 280 °C at a feed rate of 2.92 kg h^{-1} and with a 10-min residence time under stabilized temperature conditions. At the outlet of the heated screw, the torrefied biomass was conveyed into a cooled screw before being recovered as the solid phase. The gases produced by the torrefaction process were channelled into a double-wall condenser with glycol water at 5 °C to recover the liquid phase (or the oil phase, also including water content present in the biomass). The non-condensable gas (called syngas in this study) was sent to a gas analyser (GEIT GAS 3100R, Clean Air Europe®, France) to measure CO, CO_2, H_2, CH_4, C_nH_m and O_2 concentrations. The lower heating value was calculated continuously. After analysis, the syngas was burned in a thermal oxidizer at 750 °C. Torrefaction yields were determined using the ratio of the product mass to the initial dry matter mass.

2.2.2 Intermediate milling of the control sample.
Before fine milling, control powder (non-torrefied coarse-milled powder) was oven-dried at 60 °C to reach 3% moisture content then milled with an impact mill (Hosakawa Alpine UPZ 100, Hosokawa, Japan) equipped with a 0.3-mm sieving grid and fed at a rate of 1.5 kg h^{-1} *via* a twin-screw dosing system.[14] As the final aim of the study was to reduce total energy consumption of the process, the torrefied straw was not intermediate-milled in order to not add a further energy-consuming milling step.

2.2.3 Fine milling protocol.
All samples were first dried at 60 °C in an oven for 24 hours to adjust the moisture content to approximately 3%. Before milling, the moisture content was verified by weight loss after drying in an oven for 2 hours at 135 °C according to the standard ISO 711. The control and torrefied samples were fine-milled in a stirred ball mill (SBM), which Rajaonarivony *et al.* (2021)[14] determined was the most efficient tool for size-reducing wheat straw. The SBM delivers concomitant impact and attrition mechanical stress to the material. The milling conditions used here for control and torrefied wheat straw samples were the same as those described previously, with a filling rate (biomass + milling media) of 52%[14] and multiplying the mean power by the total milling time according to the procedure described by Rajaonarivony *et al.*[14]

2.2.4 Measurements of energy consumption.
For each processing step, the energy consumption was measured.

The instantaneous power of all the milling devices was measured using a PX 120 wattmeter (METRIX, France) connected to WattCom (USA) data acquisition software. The measurements then served to compute the mean power

demand, and milling energy consumption was determined by multiplying the mean power by the total milling time according to the procedure described by Rajaonarivony *et al.*[14]

The energy consumption of the torrefaction step was determined from the mean consumed power recorded directly by a Biogreen reactor multiplied by the residence time under stabilized temperature conditions (10 min). This measurement includes the energy consumed by all the components required for the process operation, such as the feeder unit, Spirajoule™ screw, cooled screw, refrigeration unit, regulation device, gas analyzer, and others.

2.3 Chemical characterization of the raw materials and powders

Supramolecular organization with solid-state NMR: ^{13}C CP-MAS solid-state NMR spectra were acquired and processed as previously described.[26]

Briefly, about 80 mg of each sample was rehydrated to 20–22% w/w with ultrapure water and then packed into a 4 mm-diameter rotor bed. The experiments were conducted under a contact time of 1.5 ms and an 8 s recycling delay. The 90° proton pulse was adjusted to 3.35 and 4 μs for control and torrefied wheat straw (prior to the milling), respectively.

The ^{13}C chemical shifts were attributed as per Bardet *et al.*[27] As the spectral resolution did not allow us to apply the peak associated with cellulose crystallinity Cr(Iα) (89.1 ppm), the approach developed by Larsson *et al.* (1997)[28] was adapted to evaluate cellulose crystallinity from the deconvoluted C-4 peaks in the region 78–91 ppm.[21]

Chemical shift, full width at half height, peak area, and Gaussian–Lorentzian ratio were determined using a least-squares fitting method with Peakfit® software (Systat Software Inc., USA).

Cellulose crystallinity (CrI), lateral fibril dimension (LFD), lateral fibril aggregate dimension (LFAD) and proportion of β-O-4 bonds in lignin were estimated as previously described.[26] Briefly, the area of the two broad signals was measured at 152.5 ppm, corresponding to the aromatic carbon atoms of lignin involved in β-O-4 bonds, such as the C-3 and C-5 of the S units, and at 147.5 ppm, corresponding to the same carbons but non-esterified. The abundance of β-O-4 bonds was considered representative of the entire lignin polymer.

The molar relative proportion of hemicelluloses was determined from the two peaks at 79 and 81 ppm after deconvolution of the 78–91 ppm region relating to both cellulose and hemicelluloses.

2.3.1 Biochemical composition.
All chemical analyses were performed on cryoground powders.

2.3.1.1 Polysaccharides. Total cell wall polysaccharide content was measured as previously described.[29] Briefly, 5 mg of sample (control or torrefied at 280 °C) was acid-hydrolysed with sulfuric acid, and the resulting freed neutral sugars were derived into alditol acetates and analysed on a TG-225 GC column (30 × 0.32 mm ID) using a TRACE™ ultra gas chromatography system (Thermo Scientific™; temperature: 205 °C; carrier gas: H_2). Uronic acids were quantified according to the

MHDP method. All measurements were performed in triplicate using standard sugar solution and inositol as internal standards for calibration.

2.3.1.2 Lignin. Lignin content was quantified by spectrophotometry using the acetyl bromide method (Hatfield & Fukushima, 2005) on samples of approximately 20 mg mass weight per assay.[30] All chemicals were laboratory-grade from Sigma Aldrich, and the analyses were performed based on four independent assays. Lignin content was expressed as a percentage of dry weight.

2.3.1.3 Protein. Total C and N contents of the samples were quantified *via* the Dumas method using an elemental analyser (VarioMicro, ELEMENTAR, France). Protein content was determined from N content multiplied by a 5.7 coefficient routinely applied to non-storage proteins. Experiments were run in triplicate.

2.3.1.4 Ash. Measurements were carried out based on standard ISO 2171. Briefly 2 grams of the sample were dried in an oven at 130 °C for 90 minutes to obtain the dry mass (m_s), measured through weighing. Subsequently, the sample was heated at 900 °C for 2 hours. After cooling down to room temperature inside a desiccator, the sample was weighed again to determine the residual mass (m_r). The ash content was calculated as the ratio of the residual mass to the dry mass. The experiments were conducted in duplicate.

2.4 Physical characterization of raw materials and powders

2.4.1 AFM (atomic force measurement). Stem parts of 5 mm length were cut for each sample of wheat straw and dried for 2 h in an oven at 60 °C. Then, they were embedded in a low viscosity resin (epoxy resin agar low viscosity resin (LV); Agar Scientific; UK) and stored in an oven overnight at 60 °C for the final polymerization. Transversal sections of the samples were obtained using an ultramicrotome (Leica EM UC7 rt with an M80 stereomicroscope, Leica Microsystems SAS, Nanterre, France) equipped with diamond knives (Trim, Histo and Ultra 45°, Diatome, Nidau, Switzerland) in order to get a mirroring surface. Peak-force quantitative nano-mechanical property mapping (PF-QNM) was performed on a multimode 8 atomic force microscope (Bruker) equipped with an RTESPA-525 probe (Bruker AFM Probes, Camarillo, CA, USA). A relative method was used to calibrate the tip and the spring constant was calculated using the Sader method.[31] The spring constant value was 215 ± 2 N m^{-1}, the resonance frequency was comprised between 500 and 522 kHz and the tip radius was fixed at 75 nm. Moreover, the peak force set-point was set at 200 nN. Images were then processed using Gwyddion software.[32]

2.4.2 Thermogravimetric analysis. Thermogravimetric analysis (TGA) was performed using a TGA2050 (TA Instruments, Waters SAS, France). Around 2 mg to 5 mg of each sample was placed in a platinum crucible and heated at 10 °C min^{-1} from ambient temperature up to 700 °C under nitrogen. Sample weight loss was recorded during heating and plotted as a function of temperature. The temperatures T1 °C and T2 °C were determined from the plot as clear degradation temperatures. Water content was determined from the weight loss at 100 °C.

2.4.3 Lower heating value measurements. The lower heating value (LHV) measurements of the powder were performed with a Parr model-6200 bomb calorimeter working to standard ISO 18125.[33] A well-known mass of the sample was introduced into the bomb calorimeter and combusted in the presence of oxygen. Hydrogen content was measured in the final analysis on an Elementar Vario Macrocube device. Moisture and hydrogen contents were measured on similar samples, and the LHV was calculated from the higher heating value (HHV) according to eqn (1) (on a dry basis). All values are expressed in J g^{-1} of dry weight. Experiments were carried out in duplicate.

$$LHV = HHV - (212 \times X) \tag{1}$$

where X is hydrogen content expressed as a percentage of dry matter.

2.4.4 Particle size distribution and agglomeration potential. The particle size distribution of the ground powders and their specific surface areas (SSAs) were first measured in ethanol (96% v/v) on a Mastersizer 2000 laser diffraction granulometer (LG) (Malvern, UK) equipped with a Hydro 2000 S system. To estimate the agglomeration state, the powder was de-agglomerated employing an embedded Mastersizer Hydro 2000 S ultrasound de-agglomerating system, and a 3-min sonification sequence was applied at maximum probe power (75 W) to a suspension of approximately 0.1 g of powder in 200 mL of ethanol previously dispersed in the Hydro 2000 S system. The suspension was then stirred at 3000 rpm for 5 minutes to remove any bubbles prior to a fresh particle size measurement. All measurements were carried out in duplicate, and the data were processed following Mie theory using the refractive index of wood sawdust (Ir = 1.53).[34] The SSA of the powder was determined from particle size distribution before and after de-agglomeration treatment and written as SSA and SSAD_LG, respectively.

The span, which is an expression of the width of the distribution, was also calculated based on eqn (2), where d_{10}, d_{50} and d_{90} are the 10th, 50th and 90th percentiles of the particle size distribution (PSD), respectively.

$$span = \frac{d_{90} - d_{10}}{d_{50}} \tag{2}$$

2.4.5 Grindability of the samples. To assess the grindability of the samples (control wheat straw oven-dried overnight at 105 °C, the 220 °C-torrefied and the 280 °C-torrefied wheat straw), milling kinetics tests were carried out in a small-scale reciprocating impact mill (MM400, Retsch®, Germany) as described by Rajaonarivony *et al.* (2019) with the aim of comparing the time–course of size reduction and agglomeration.[35] The samples were milled after the coarse milling step. Thus, the control sample was not passed through the intermediate milling step. Two opposite 50-mL bowls were each filled with one 25-mm-diameter ball of 63 g and with 1.8 g of sample. The bowls were shaken at 20 Hz frequency up to a total milling time of 140 min. Subsamples were recovered from the bowls at various intervals and analyzed as described in section 1.6, and

SSA was calculated from the particle size distribution. The SSA was then plotted as a function of milling time, and grindability was evaluated as the slope of the linear regression of the linear part of the curve (corresponding to the early stages of grinding).

2.4.6 Particle shape measurements. Particle shape measurements were performed using a Morphologi 4 granulomorphometer (Malvern, UK) in dry mode. Briefly, 5 mm³ of control powder and 11 mm³ of 280 °C-torrefied powder were dispersed on a plate using the dry module of the device (air pressure: 1 bar; injection time: 20 ms; settling time: 60 s). The particles below and larger than 20 microns were analysed at ×20 and ×10 magnification respectively. A z-stack of two or three images was applied during the acquisition for the control or torrefied powder, respectively. In order to analyse at least 100 000 particles per sample, we defined 3 sampling zones per plate and then merged the results to determine the shape factors. As the median particle size of the powder was 20 μm, global distributions were constructed by post-processing, as described in previous work, by considering that particles below 20 μm and above 20 μm each accounted for 50% of the total.[16]

Particle elongation and convexity were determined from the images according to eqn 3

$$el = 1 - \frac{W}{L} \tag{3}$$

where W and L are the maximum width and maximum length of the particles, respectively. An elongation of 0 corresponds to a perfectly round or cubic particle, and an elongation of 1 corresponds to an infinitely elongated particle (with no width).

Convexity was also calculated as the ratio of the convex hull (the smallest convex polygon that contains all the vertex of the particle) to the perimeter of the particle (eqn 4)

$$Con = \frac{\text{convex hull perimeter}}{\text{perimeter of the particle}} \tag{4}$$

The calculated convexity gives an indication of the particle surface condition: a perfectly smooth particle will have a convexity of 1.

2.4.7 Flowability. The flow properties of the powders (280 °C-torrefied and control) were quantified using an FT4 powder rheometer (Freeman, Technology, UK) via compressibility, cohesion and basic flowability energy (BFE) tests according to protocols defined by Freeman,[36] as described below. Before each measurement, the powders were oven-dried at 60 °C for 24 hours to eliminate the influence of water adsorbed onto the surface of the particles.

2.4.8 Cohesion (Co). A 85-mL vessel was filled with the powder. The powder bed was first homogenized by displacement of the rotary blade through the entire height of the powder bed (named 'conditioning step') and then consolidated by applying a normal stress (perpendicular to the surface) of 3 kPa. The torque required to shear the consolidated powder bed under 5 increasing normal stresses (from 1 to 2 kPa) was measured, and shear stress was then linearly fitted using the Mohr–Coulomb method:

$$\tau(\sigma) = Co + F\sigma. \tag{5}$$

where τ is shear stress (kPa), F is static friction coefficient, σ is normal stress (kPa), and Co is cohesion (kPa). The cohesion value (Co) is the y-intercept of the regression line with the y-axis.

2.4.9 Compressibility. The compressibility of a powder is the ability of the powder bed to decrease in volume under the action of normal mechanical constraints. Compressibility measurements were performed using the device's 85-mL vessel filled with the powder. The powder was homogenized as previously described (conditioning step), and then a series of 9 normal stresses increasing from 0.5 kPa to 15 kPa were successively applied. The final height of the powder bed (i.e. at a normal stress of 15 kPa) was measured, and compressibility was then calculated according to eqn (6), where V_i is initial volume of the powder bed in the vessel and $V_{15\ kPa}$ is the final volume of the powder

$$Cp = \frac{V_i - V_{15\ kPa}}{V_i} \times 100 \tag{6}$$

3 Results and discussion

3.1 Effects of the torrefaction step on the physical and chemical properties of wheat straw

The wheat straw (WS) to be torrefied was in the form of coarse-milled particles. The particle size distribution of the particles has a $d_{10} = 182$ μm, $d_{50} = 600$ μm, and $d_{90} = 1254$ μm. The torrefaction was carried out at 220 °C and 280 °C for 10 min under nitrogen flushing in the Biogreen reactor.

3.1.1 Influence of the biochemical composition. The biochemical composition of the different samples is given in Table 1. Cellulose is assimilated to the anhydro-glucose content that is resistant to mild hydrolysis, and (arabino)xylans correspond to the sum of the residues arabinose and xylose. The control (wheat straw, i.e. WS) is mainly composed of cellulose (29.8 ± 0.5 g/100 g), (arabino)xylans (24.5 ± 0.3 g/100 g) and lignins (23 ± 0.1 g/100 g). These data are consistent with the composition of wheat straw described in previous studies.[37]

The 220 °C-torrefaction step affected the composition of wheat straw very slightly whereas the 280 °C-torrefaction step led to a 67% increase in protein, a 116% increase in lignin and a 28% decrease in cell wall polysaccharides.

Analysis of the monosaccharide composition of cell wall polysaccharides showed that non-cellulosic polysaccharides were more sensitive to thermolysis (cell wall polysaccharides, i.e. CWP residues, Table 1) than the cellulosic ones. In particular, the proportions of xylose, arabinose and galactose residues decreased by 65%, 54% and 71%, respectively, after the 280 °C-torrefaction.

The CrI (crystallinity index) by NMR was calculated according to Larsson et al. (1997),[28] along with other methods that integrate the hemicellulose signal in the amorphous cellulose part. The spectra obtained for the different samples are shown in Fig. 2.

Table 1 Chemical composition (g/100 g) of proteins, lignins and cell wall polysaccharides (CWPs) in the control and torrefied wheat straw samples, crystallinity and fiber dimensions and thermal transition temperature and mass loss measured by TGA

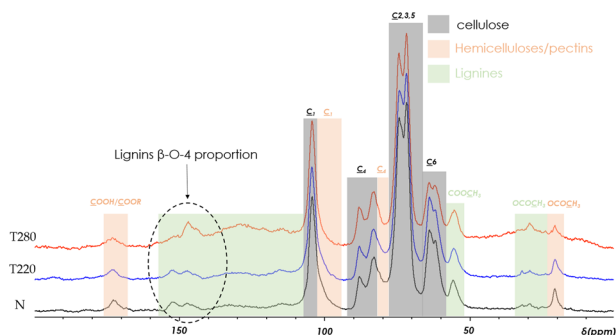|	WS	220 °C-TWS	280°C-TWS
	Control	Torrified wheat straw at 220 °C	Torrified wheat straw at 280 °C
Protein	4.3 ± 0.1	4.5 ± 0.1	5.3 ± 0.1
Lignin	23.0 ± 0.1	27.9 ± 0.1	47.9 ± 0.1
Ash	5.39 ± 0.06	5.39 ± 0.36	7.44 ± 0.191
Total CWP	**65.5 ± 1.25**	**62.7 ± 1.38**	**46.8 ± 0.61**
CWP residues			
Rha (rhamnose)	0.29 ± 0.09	0.23 ± 0.05	0.14 ± 0.04
Ara (arabinose)	3.7 ± 0.23	4.0 ± 0.09	1.7 ± 0.2
Xyl (xylose)	20.8 ± 0.24	19.9 ± 0.71	7.4 ± 0.08
Man (mannose)	0.77 ± 0.11	0.95 ± 0.02	0.41 ± 0.1
Gal (galactose)	0.79 ± 0.2	0.73 ± 0.03	0.23 ± 0.1
Glc (glucose)	35.4 ± 0.49	33.6 ± 0.74	34.4 ± 0.39
UA (uronic acid)	3.7 ± 0.22	3.3 ± 0.07	2.6 ± 0.08
Main CWPs	*54.3 ± 0.76*	*53.6 ± 1.32*	*39.1 ± 1.32*
Cellulose	29.8 ± 0.47	29.7 ± 0.56	30 ± 1.1
Arabinose (xylan)	24.5 ± 0.29	23.9 ± 0.76	9.1 ± 0.22
Cellulose crystallinity (%)	35 ± 1	$38\% \pm 1$	38 ± 1
Total crystallinity (including hemicellulose)	25 ± 1	27 ± 1	32 ± 1
LFD (nm)	2.8	3.0	3.0
LFAD (nm)	26.4	25.1	30.9
Estimated β–O–4 bonds (%)	47 ± 1	40 ± 1	36 ± 1
Proportion of hemicellulose in (CWP)	29 ± 1	30 ± 1	16 ± 1
W_c (%)	6.6	5.5	3.3
T1 (°C)	$270° \pm 1$	$278 °C \pm 0$	$291 °C \pm 0$
T2 (°C)	$448° \pm 3$	$441° \pm 0$	$456° \pm 1$
Mass loss at 220 °C	$9.9\% \pm 0.5\%$		
Mass loss at 280 °C	$22.0\% \pm 0.9\%$		

Spectra show signals in the zone associated with polysachharides (60–110 ppm). Most of the signals correspond to cellulose (grey areas), but signals associated with hemicelluloses and pectins are also present (orange areas). Finally, signals characteristic of lignins are found in the 110–160 ppm zone. CrI values (Table 1) show a slight but significant[38] increase for the torrefied samples regardless of the calculation method used. Comparison of the CrI values resulting from the different calculation methods highlights a greater degradation of the hemicelluloses than the celluloses, relating to the higher molar proportion of hemicelluloses.

Fig. 2 NMR spectra for the control (N), 220 °C-torrified WS (T220) and 280 °C torrefied wheat straw (T280).

The amorphous region of the cellulose, which is the major part, is known to be the cellulose fraction that is most sensitive to thermal degradation. Here, the higher final CrI indicates that the cellulose decrease observed in global biochemical analyses is mainly due to the thermal degradation of the amorphous region.

The LFD (lateral fibril dimension) remained constant during the torrefaction process, whereas the LFAD (lateral fibril aggregate dimension) increased. One hypothesis is that the cellulose aggregates collapse during the torrefaction process. Indeed, the degradation of amorphous parts could expose some crystalline regions on the surface of the aggregates, allowing them to interact and form aggregates with a larger cross-section.

The proportion of specific covalent linkages, such as β–O–4 bonds in the lignin fraction, which are representative of the entire lignin ultrastructure, decreases as a function of torrefaction temperature. This decrease can be attributed to a breakdown of the lignin network, as previously reported by Wen *et al.*[39] In addition, the decrease in the proportion of hemicellulose (measured in moles in solid state NMR analysis) is well correlated with the decrease in arabinose, xylose, galactose and mannose measured by biochemical analyses in weight.

3.1.2 Thermal analysis. Table 1 shows the degradation temperature and corresponding mass losses measured by thermogravimetric analysis for the control (WS) and the 220 °C

and 280 °C-torrefied samples. The water content of the control was moderate (6.6% of dry mass) but higher than that of the TWS, especially for the 280 °C-torrefied sample. This can be explained by the partial degradation of more than 50% of the hydroxyl group-rich hemicelluloses (44.3% of hemicellulose in WS against 21% in the 280 °C-TWS), leading to a decrease in the number of water-bond sites that can interact with water in TWS.

The mass losses observed at 220 °C and 280 °C were 9.9% ± 0.5% and 22.0% ± 0.9% respectively, corresponding to a net mass loss of 3.3% and 15.6% after deducting the water content. The weak mass loss at 220 °C is consistent with the low levels of chemical degradation observed at the same temperature. Interestingly, the mass loss at 280 °C is in the same range as the difference in the content of the main CWP(s) measured by the biochemical analyses (54.3 − 39.1 = 15.1%) reinforcing the reliability of both measurements.

3.1.3 Thermal induced modifications at the cell wall scale. Fig. 3 shows the indentation modulus mapping produced by AFM PF-QNM on the control, (initial state-Fig. 3a), and after heat treatment at 220 °C (Fig. 3b and c) and 280 °C (Fig. 3d and e). First of all, in terms of cell morphology, AFM images show a significant alteration of the cell walls at a temperature of 280 °C; the cells seem to have lost their integrity. AFM mapping is supplemented by Table 2, which shows the average values recorded in the cell walls and in the middle lamella zones.

It should be noted that in contact mechanics, indentation properties are calculated from a theoretical contact area which is not always consistent with experimental reality. Here, the indentation modulus values found in the cell walls are around 15 GPa for the raw samples and those treated at 220 °C; these values are consistent with the values found in the literature for wood fibres that have similarities to the cells studied here, particularly in terms of xylose content.[40] One can notice a significant drop in the mechanical properties after 280 °C

Table 2 Indentation modulus values obtained for the control and the 220 °C and 280 °C torrefied samples for the cell walls and middle lamellae regions

	Cell wall region	Middle lamella
Control	14.9 ± 5.3 GPa	12.3 ± 5.2 GPa
220 °C torrefied sample	15.5 ± 2.3 GPa	10.9 ± 1.1 GPa
280 °C torrefied sample	10.7 ± 1.8 GPa	N.D.

exposure. This is well correlated with the behavior observed on other plant fibres such as flax cell walls.[41]

This drop can be attributed to the development of porosities within the cell wall due to the decrease in non-cellulosic polymers previously reported and the increase in the LFAD distance. This led to a decrease in cell wall density and consequently a loss in terms of mechanical properties. Interestingly, the AFM PF-QNM technique is resolutive enough for calculating stiffness values in local regions such as the middle lamellae. Here, values between 9 and 12 GPa are calculated in these areas. These values are fully in line with the CML indentation modulus obtained in CML regions of different xylan-type fibre bundles such as jute or kenaf.[42] After being treated at 280 °C, morphological damage occurs on the cell wall, making it difficult to clearly identify the middle lamella. This explains why no value is reported for the 280 °C torrefied sample.

In general, morphological and mechanical assessments confirm the previous biochemical and structural results obtained through NMR and biochemistry, providing insights into the histological degradation of the straw. This also suggests a potential modification in the grindability of the materials. Cross-sectionally, this also demonstrates the high potential of AFM PF-QNM for a localised and highly resolving investigation of plant cell wall stiffness and microstructure.
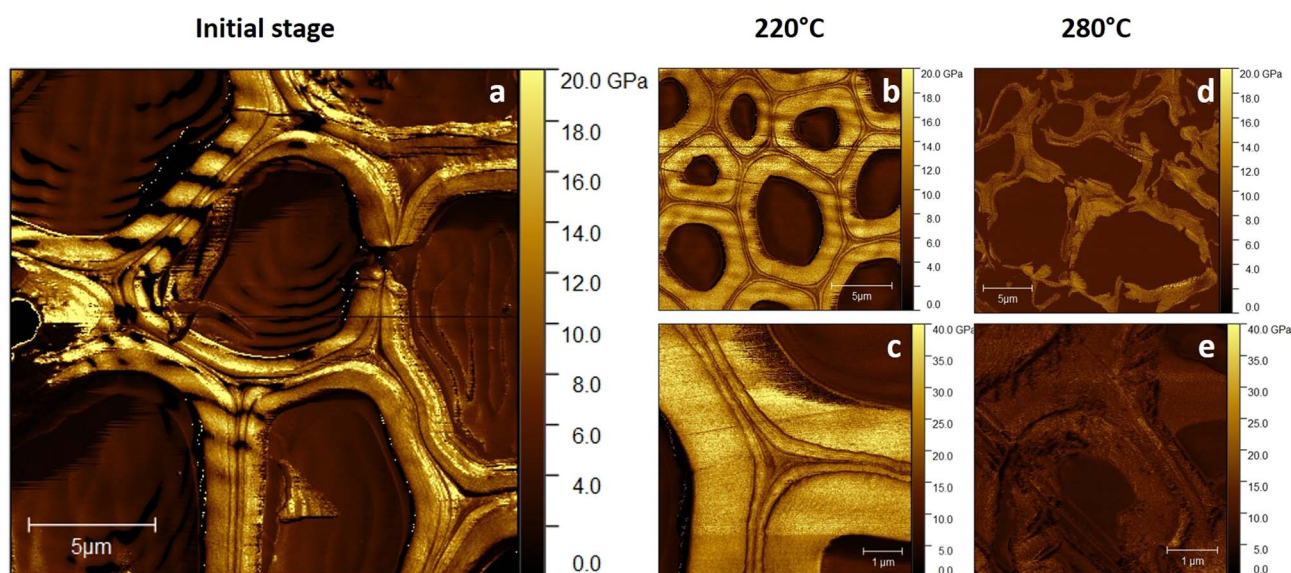

Fig. 3 Indentation modulus mapping for control (WS) wheat straw cell walls (a), treated at 220 °C (b) and 280 °C (d). A focus on the middle lamellae region is also proposed on 220 °C (c) and 280 °C (e) samples.

3.1.4 Grindability and agglomeration of the torrefied wheat straw.

Fig. 4a shows the evolution of the specific surface area (SSA) with milling time, for the control (WS), 220 °C torrefied (220 TWS), and 280 °C torrefied wheat straw (280 TWS). The first point to note is that the size reduction kinetics was faster for the 280 °C TWS compared to the control (WS) and the 220 °C TWS. Based on the Rittinger law, which states that the surface area created is directly proportional to the energy injected into the milling machine,[43] we determined the grindability of each sample as the slope of the linear regression on the first part of the SSA measurement curve. This was calculated for time in between 0 and 20 min for controls and 220 °C TWS and from 0 to 15 min for torrefied samples (corresponding to the most linear part of the curve). The values and regression coefficients are reported in Table 3. The regression coefficient, which was found to be greater than 0.90, indicates that agglomeration does not dominate over the comminution phenomena in the initial stage of the milling.

The grindability of the control and the 220 °C TWS is quite close (0.51 and 0.46 $m^2 g^{-1} min^{-1}$) and half those of the 280 °C TWS. This reveals an effect of fragilization of the material due to the thermal treatment at the highest temperature, as previously highlighted through AFM PF-QNM mapping. The degradation of some part of the lignocellulosic matrix, 15% in mass, in particular the hemicelluloses and amorphous cellulose creates microvoids in the cell wall and middle lamella structure that can serve as areas for initiation and propagation of fracture paths.

The evolution of the specific area over time can also be used to determine the agglomeration potential of the powders.[44] Two types of agglomeration are generally distinguished.[45]

Reversible agglomeration, also known as soft agglomeration, can be assessed using the specific surface area that is released after applying ultrasonic treatment (UT), which allows the powder to de-agglomerate. Reversible agglomeration hampers the efficiency of the milling process but does not completely impede comminution. In contrast, irreversible agglomeration (hard agglomeration) occurs due to stronger interactions between biomass particles that cannot be broken by UT. Hard

Table 3 Grindability of control (WS) and torrefied wheat straw (TWS) at the lab scale

	Grindability ($m^2 g^{-1} min^{-1}$)	R^2
WS (control)	0.051	0.90
220 °C-TWS	0.046	0.91
280 °C-TWS	0.112	0.94

agglomeration is evident when the specific surface area decreases with increasing milling time after UT treatment (*i.e.*, particle size increases).[14]

In Fig. 4a, we observe a plateau for the SSA, which can be attributed to the presence of agglomeration phenomena that compete with comminution. As shown in Fig. 4b, for longer milling times, the SSA_{D-LG} value decreased for both the 280 °C torrefied wheat samples (starting from 20 minutes of milling) and the 220 °C torrefied wheat samples (starting from 60 minutes of milling), highlighting the presence of strong agglomeration. Interestingly, no irreversible agglomeration is observed in the control sample. While we do not know, currently, the exact origin for these interactions responsible for hard agglomeration, we can assume that the biochemical changes generated by torrefaction make certain chemical groups more accessible. These groups are then more likely to form stronger interactions with others.

Agglomeration is mainly governed by the ratio of interparticle forces (van der Waals forces, hydrogen bonds, and possibly covalent bonds due to the effects of mechanochemistry on gravity). These are related to the chemical surface composition of the particles, which is modified during the torrefaction process. Additionally, as the torrefaction process increases grindability, it also leads to an increase in the proportion of the smallest particles and stronger agglomeration, particularly in the case of the 280 °C temperature.

Therefore, the modification in the cellular structure observed with AFM at the 280 °C torrefaction temperature
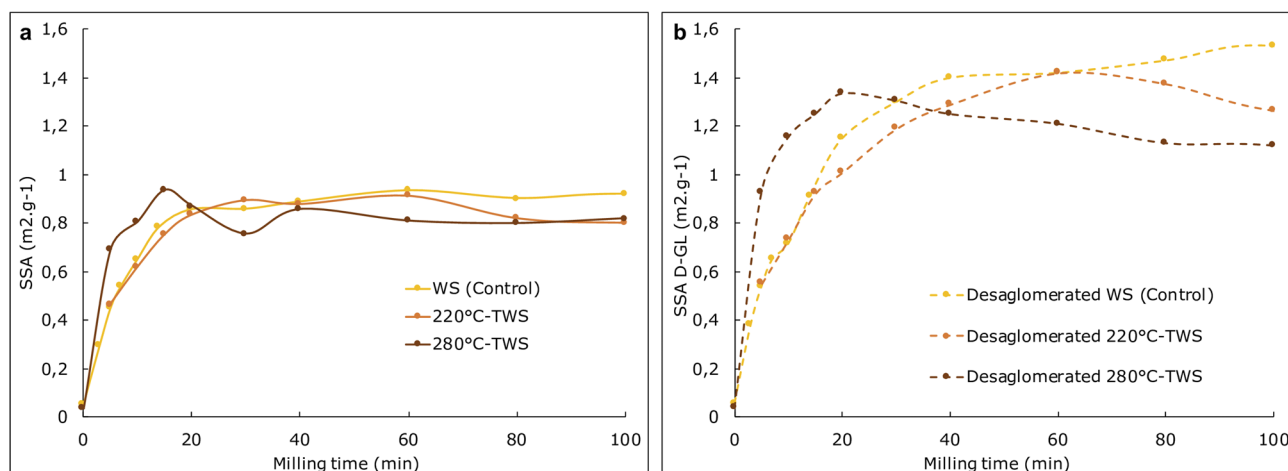

Fig. 4 Evolution of specific surface area before (plain line, Fig. 2a)) and after (dashed line, Fig. 2b) de-agglomeration with ultrasonic treatment (UT) in control (WS) and torrefied samples (220 °C TWS and 280 °C-TWS) in a lab-scale MM400 ball-mill.

effectively leads to higher grindability. On the other hand, torrefaction also increases the total agglomeration regardless of the temperature considered.

3.2 Milling in a pilot-scale stirred ball mill and powder properties

3.2.1 Milling time. In the previous sections, our results showed that torrefaction at 220 °C did not result in significant changes in the chemical and structural properties of wheat straw. The grindability was not significantly improved either. However, this treatment primarily seems to affect the surface composition, as it leads to a significant increase in agglomeration. On the other hand, torrefaction at 280 °C resulted in more significant modifications in the physicochemical properties of the wheat straw and a clear improvement in grindability, even though agglomeration forces were strengthened. Therefore, the second part of this work, the study of grindability and powder properties, was specifically conducted on the powders obtained through the thermal treatment at 280 °C.

The coarsely milled and torrefied powders were finely milled in a pilot-scale stirred ball mill (SBM) to reach a target mean particle size of 20 μm, which is the target particle size for feeding an internal combustion engine.[42] The 280 °C-torrefied wheat straw powders were compared in terms of milling behaviour to the control samples that had been prepared with intermediate impact grinding in the UPZ mill instead of the torrefaction step.

Table 4 reports the main particle size characteristics of the sample prior to milling. As the control was submitted to an additional milling step, the d_{10}, d_{50}, and d_{90} values of torrefied straw powders were logically 35–40% higher than those of the controls. The span reflecting the spread of the distribution was similar between control and torrefied samples.

In the SBM, the milling time to reach a median particle size of $d_{50} = 20$ μm was 96 min and 16.8 min for the control and 280 °C-TWS respectively, *i.e.* a time reduction of more than 80% for the torrefied sample. This reduction is especially significant given that TWS had particles that were coarser (around 40%, see Table 4) than the control.

3.2.2 Particle size distribution. Fig. 5 compares the particle size distribution profiles between the milled control sample and the 280 °C TWS samples. The main characteristics of particle size are also reported in Table 4. The 280 °C TWS exhibits a slightly different profile compared to the control sample: a higher span (5.9 *vs.* 4.6) and d_{90} value (123 *vs.* 97 μm), indicating larger particle sizes of the feedstock material. It is worth noting that the 280 °C TWS has fewer particles in the range of 0.2–2.5 μm and shows a shoulder in the 200–600 μm region ($d_{10} = 2.6$ μm for WS and $d_{10} = 3.3$ μm for TWS). This pattern is typical of the agglomeration phenomenon discussed previously. The finer particles either agglomerate among themselves or with larger particles, resulting in the generation of particles of greater sizes, which explains the noticeable shoulder in the 200–600 μm range.

3.2.3 Particle shape. As the spread of the particle size distribution does not afford an accurate focus with the same magnification for particles below and above 20 microns, elongation and convexity were measured separately and reported in

Table 4 Main granulometric features of control and torrefied wheat straw before and after milling

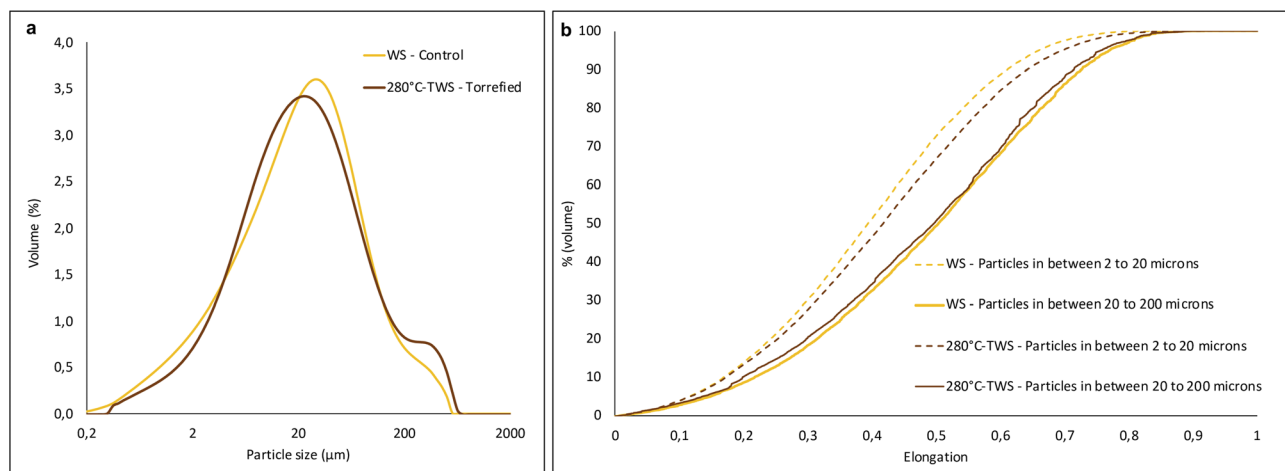|		SSA, m² g⁻¹	d_{10}, μm	d_{50}, μm	d_{90}, μm	Span
Before fine milling	WS	0.055	64	286	691	2.2
	280 °C-TWS	0.037	98	478	1102	2.1
After fine milling	WS	0.831	2.6	20.5	97.3	5.9
	280 °C-TWS	1.017	3.3	20.1	122.8	4.6

Fig. 5 Particle size distribution (a) and cumulative elongation distribution for particles below 20 μm (b) for control (WS) and torrefied wheat straw (TWS) after milling.

Fig. 5b (cumulative distribution). An elongation around 1 corresponds to very elongated particles, whereas an elongation equal to 0 corresponds to perfectly square or round particles. The main particle shape indicators are reported in Table 5 and the elongation distributions are plotted in Fig. 5b for WS-milled control and the 280 °C TWS samples.

For the coarser particles (above 20 microns), the elongation distributions of the WS and the 208 °C-TWS powders were very close, with a median elongation of around 0.5 which corresponds to a length twice as large as the width. For the smaller particles, the WS powder showed lower median elongation (0.39) than 280 °C-TWS (0.42). This difference can be related to the shorter milling time of the 280 °C-TWS. Due to its higher grindability, the 280 °C-TWS powder had a lower residence time than control powder. The 280 °C-TWS powder was thus less rounded by the mill ball and kept its shape factor.

Convexity values showed little difference between finer (below 20 μm) and coarser particles (above 20 μm) for the control sample. The coarser particles appeared to be a little smoother than the smaller particles. However, the torrefied sample showed the opposite pattern, and the gap between the values for particles below and above 20 microns was much greater. Thus, in this case, the smaller particles were smoother and the coarser ones exhibited more shape irregularity. Many factors may explain this difference. First, similar observations were previously reported for powders obtained using a milling device that worked predominantly with attrition as the main mechanical force.[16] As the input torrefied particles had skipped the intermediate milling step, the ratio between size of the milling media and size of the particles was lower for 280 °C TWS than for the control. This would lead to a better efficiency of the attrition mode in comparison to the impact loading mode generated by the device, which could explain these observations. In addition, due to the shorter residence time needed in the mill to reach the target particle size, the coarser particles are less polished by the grinding media. The torrefaction process also degrades some components (hemicellulose and amorphous cellulose) and could generate microvoids inside the torrefied particles. The preferential propagation of fracture paths through these microvoids could lead to the formation of irregular coarse particles.

We also demonstrated that the 280 °C-TWS powder has a greater tendency to agglomerate than the control, and agglomerates generally exhibit smoother and more regular shapes.

3.2.4 Flow properties of torrefied and SBM-milled wheat straw powders. For combustion application in engines, the lignocellulosic biomass needs to be conveyed and injected under pressure, which means that its flowability properties are an essential factor in ensuring a regular feed into the engine and avoiding clogging and vaulting phenomena.[6] Flowability is mainly related to physical factors such as the size, shape and surface compositions of particles and can be modified by thermal treatment.[46] The flowability can be evaluated with various indicators. Here we focused on two of them measured: compressibility and cohesion. The results are shown in Table 6.

Compressibility is an indicator that quantifies the changes in density of a powder when a normal stress is applied. Compressibility is often compared to the Carr index, which expresses the compressibility of a powder when self-arranged after tapping down (i.e. under its own weight).[47]

The control WS had a compressibility of about 36% whereas the ground 280 °C TWS was less compressible with a value of 32%. If we compare the value obtained to the Carr index reference table, the torrefaction step moved the ground straw from the range of a very-poor-flowability powder (35–38%) to the range of a poor-flowability powder (28–35% compression).[47] In practice, this index was defined to quantify the flow of a powder under quasi-static conditions, which refers to the flow of a powder under its own weight. In the context of high-power energy applications, achieving good flowability isn't strictly required, as forces are employed to set the powder in motion. However, even slight improvements, like this one, will facilitate the handling of the powder since less significant mechanical forces are needed to initiate the movement of the particles.

Compressibility is affected by the deformability of the particles. Under a normal stress, a deformable particle can fill any voids in the powder bed.[48] The torrefaction process makes the straw particles more brittle (as shown by the increase in grindability), which decreases their deformability and thus the compressibility of the powder.

Cohesion was halved by the torrefaction process, shifting from 0.42 to 0.22 kPa. Cohesion can be seen as a measure of the intensity of inter-particle forces, which depends on the interactions between chemical groups and the physical defects at the surface of the particles and is also related to the distance between particles. All the powders here had the same d_{50} (~20 μm), and we showed in Table 4 that the 280 °C torrefied powder had a higher d_{10} than the control (WS), which can be assimilated to a lower presence of smaller particles in the torrefied sample, probably due to the formation of agglomerates and

Table 5 Median elongation and convexity values for control and torrefied wheat straw powders

		Elongation			Convexity		
		El_{10}	El_{50}	El_{90}	Con_{10}	Con_{50}	Con_{90}
Control (WS)	Particles < 20 μm	0.17	0.39	0.61	0.64	0.75	0.87
	Particles > 20 μm	0.22	0.50	0.72	0.63	0.78	0.91
280 °C-TWS	Particles < 20 μm	0.17	0.42	0.61	0.75	0.89	0.98
	Particles above 20 μm	0.20	0.50	0.71	0.56	0.72	0.88

Table 6 Compressibility (%) and cohesion (kPa) of control and 280 °C TWS samples

	Comp. (%)	Co (kPa)
Control (WS)	36.1 ± 0.5%	0.42 ± 0.1
280 °C -TWS	32.1 ± 0.7%	0.22 ± 0.6

a smoothing effect of the particle surface (see convexity values), thus decreasing the cohesion in the powder which flowed as it was made up of larger particles.

In lignocellulosic materials, it is widely agreed that hemicelluloses are hydrogen-bonded to cellulose and covalently bonded to lignins.[49,50] The non-cellulosic components are strongly correlated with the cohesive forces within the cell wall of lignocellulosic materials. Studies have shown that the branches of xylan hemicelluloses such as arabinose, glucuronic acid or acetyl are responsible for these interactions by coordinating to hydrogen bond donor sites on the cellulose surface.[51,52] Here, we found that the torrefaction process preferentially degraded the arabinoxylans. Again, we can assume that this decreases such interactions in the torrefied particles and leads to a decrease in inter-particle forces. The hydrophilizing effect of the powders conferred by the torrefaction treatment due to the elimination of such hydrophilic compounds would most likely further drive this decrease. Finally, torrefaction also leads to a densification of the matter (*i.e.*, particles of the same size are heavier after the torrefaction step) and the chemical modifications of the lignocellulosic biomass due to the torrefaction process may significantly decrease the inter-particle force/weight decrease ratio, leading to a decrease in cohesion.

3.3 Energy balance and overall advantages of the torrefaction process

3.3.1 Yields of the torrefaction step. Table 7 summarises the yields of the torrefaction steps and thermal properties of the products obtained. The torrefaction step leads to a total mass loss of 30% corresponding to the yield in oil (23.33%) and syngas (6.67%). The oil yield corresponds to the condensable part of the gases released (including the adsorbed, absorbed and biomass-constitutive water). The syngas, the non-condensable part of the gases produced, is mostly CO and CO_2 with a minor amount of alkanes.

The lower heating value of the 280 °C_TWS shows an increase of 22% compared to that of the control (before the torrefaction). This reflects the concentration of energy in the torrefied powder. The energy yield (E_y) in the torrefied biomass was defined as the ratio of the energy content in the torrefied samples to the energy content of the raw biomass:

$$E_y = \frac{LHV_{TWS} * Y}{LHV_{WS}}$$

where LHV_{TWS} and LHV_{WS} are the LHVs of 280 °C-TWS and the raw WS, respectively, and Y is the yield in torrefied biomass ($kg_{torrefied\_biomass}/kg_{raw\_materials}$). The TWS had an energy yield of 90%, which is a relatively good yield for the targeted combustion applications, as most of the energy of the raw biomass is concentrated in the torrefied powder.

3.3.2 Energy consumption in the different process steps. The energy consumption in each step of the production of the 280 °C-TWS ground powder has been calculated for 1 ton of biomass entering the process and is reported in Table 8.

The energy consumption reported here for fine milling takes into account the yield of biochar after the torrefaction step (70%). In a similar way, residual energy was calculated from the LHV multiplied by the yield of the torrefaction step. Table 8 also reports the residual energy and the energy return on investment (EROI) for control and torrefied samples which is defined as the amount of energy in the products divided by the amount of energy provided to the process.[55] In this case, the EROI was calculated as the ratio of residual energy to total energy consumption for 1 ton of input biomass feedstock. The first point to note is that the total energy consumption was relatively similar (less than 2% difference) between control and torrefied samples (1598.7 *vs.* 1626.6 kW h t^{-1}). Indeed, the significant energy gain obtained during the grinding step is offset by the energy cost of torrefaction.

During our experimentation, we measured an energy consumption of 1360 kW h t^{-1} (dry basis) for the torrefaction step, with a residence time of 10 minutes inside the reactor. This value appears to be high, around 5 to 7 times higher than other values reported in the literature (~200 kW h t^{-1}) for torrefaction of lignocellulosic biomass.[53–56] The difference can be attributed to the low density of wheat straw and the fact that the energy consumption measurements in this study take into account the total consumption of the pilot reactor, including its peripherals. Additionally, it should be noted that this

Table 7 Torrefaction yield and product property summary

Yields	
Solid matter (280 °-TWS)	70%
Oil	23.33%
Syngas	6.67%
Properties of torrefaction's products	
Lower heating value (LHV) of raw WS	15.2 MJ kg^{-1} of dry matter
Lower heating value (LHV) of 280 °C-TWS	19.5 MJ kg^{-1} of dry matter
Main compound present in the syngas	CO_2: 30.83%
	CO: 16.71%
	Alkane: 5.37%
Lower heating value (LHV) of syngas	4.63 MJ m^{-3}

Table 8 Energy consumption, residual energy, and energy return on investment (EROI) for control and torrefied wheat straw

Energy consumption	WS	280 °C-TWS
Coarse milling (kW h t^{-1})	49.2	49.2
Torrefaction (kW h t^{-1})	—	1360
Intermediate milling (kW h t^{-1})	181.5	—
Fine milling (kW h t^{-1})	1368	217
Total energy consumption (kW h t^{-1})	1598.7	1626.6
Residual energy (kW h t^{-1})	4222.2	3802.4
EROI	2.64	2.33

experimental torrefaction operation was not optimized for industrial process practice.

In an industrial process, we can expect to significantly reduce the total energy consumption needed for production of the 280 °C sample by optimizing the torrefaction step, which was not the purpose of this study. Currently the values measured for this step are 5 to 7 times higher than those in the literature. A simple 2-fold reduction of the torrefaction energy leads to an EROI of 4.1 (*i.e.* 1.5 times higher than the EROI of the WS).

In addition, this yield can be further improved by re-using the energy content in the syngas and oil to decrease the energy consumption of the torrefaction step. To give an order-of-magnitude idea, syngas yield was 22% with a LHV of 4.2×10^3 kW h m^{-3}. Assuming that the volumetric mass density of the syngas is 1–1.5 kg m^{-3}, the use of the energy contained in the syngas and oil could increase the EROI to between 2.97 and 3.28 kg m^{-3} with the current energy consumption measured for the torrefaction step, which would fully justify practical consideration of torrefaction as a pre-processing step.

In addition, torrefaction also increased the density of the materials and decreased the water uptake of the lignocellulosic biomass, thus facilitating its subsequent storage. Finally, the improvement of the flowability properties of the combustible powder facilitates its implementation in the combustion process, limiting potential blocking points during conveying and enabling better regulation of the feedstock feed, leading to better-quality energy recovery.

4. Conclusions

In this study, we explored the potential benefits of torrefaction as a pre-treatment before fine-milling wheat straw, with a specific focus on its applicability to produce powdered fuel intended for high-power energy applications. Our research indicates that a torrefaction temperature of 220 °C for 10 minutes is insufficient to bring about significant structural changes in the physical and chemical properties of wheat straw. In contrast, at a higher temperature of 280 °C, notable structural transformations occur, which have a substantial impact on both the grindability of the raw material and the rheological properties of the resulting powder. While the energy return on investment (EROI) is relatively consistent regardless of whether the wheat straw is raw or torrefied, there is untapped potential for enhancing the EROI by optimizing the energy efficiency of the torrefaction process and by capitalizing on the energy contained in the by-products of torrefaction. From an industrial perspective, torrefied powders offer distinct advantages, such as increased energy density and improved flow properties. These findings suggest that torrefaction could offer significant benefits in the biomass-to-energy value chain, especially for high-power energy applications.

Abbreviations

BFE	Basic flow energy
Co	Cohesion
Con	Convexity
Cp	Compressibility
CrI	Crystallinity index
CWPs	Cell wall polysaccharides
d_{10}, d_{50}, and d_{90}	10th, 50th and 90th percentiles of particle size distribution
E_y	Energy yield
El	Elongation
EROI	Energy return on investment
LFAD	Lateral fibril aggregate dimension
LFD	Lateral fibril dimension
LHV	Lower heating value
NER	Net energy ratio
PSD	Particle size distribution
SBM	Stirred ball mill
SSA	Specific surface area
SSAD-GL	Specific surface area after an ultrasonic-treatment deagglomeration step
TWS	Torrefied wheat straw
WS	Wheat straw

Author contributions

Rova-Karine Rajaonarivony: conceptualization, investigation, formal analysis, writing – original draft, writing – review & editing. Xavier Rouau: conceptualization, funding acquisition, investigation, formal analysis, writing – original draft, writing – review & editing. Jean-Michel Commandré: methodology, investigation, writing – review & editing. Charlène Fabre: methodology, investigation, writing – review & editing. Jean-Eudes Maigret: methodology, investigation. Xavier Falourd: methodology, investigation, formal analysis, writing – review & editing. Bruno Piriou: methodology, investigation, funding acquisition, review & editing. Alain Bourmaud: methodology, investigation, writing – review & editing. Camille Goudenhooft: methodology, investigation, review & editing. Sylvie Durand: methodology, investigation, review & editing. Johnny Beaugrand: methodology, investigation, writing – review & editing. Sophie Le Gall: methodology, investigation, writing – review & editing. Claire Mayer-Laigle: conceptualization, funding acquisition, investigation, formal analysis, writing – original draft, writing – review & editing.

Conflicts of interest

The authors declare that they have no known competing financial interests or personal relationships that could have appeared to influence the work reported in this paper.

Acknowledgements

UR1268 BIA, IBiSA, Phenome-Emphasis-FR ANR-11-INBS- 0012, PROBE and CALIS infrastructures, Biogenouest).

Notes and references

1 J. Deng, et al., Pretreatment of agricultural residues for co-gasification via torrefaction, J. Anal. Appl. Pyrolysis, 2009, **86**(2), 331–337.

2 M. Mandø, et al., Pulverized straw combustion in a low-NOx multifuel burner: Modeling the transition from coal to straw, Fuel, 2010, **89**(10), 3051–3062.

3 C. Mayer-Laigle, et al., Comminution of Dry Lignocellulosic Biomass, a Review: Part I. From Fundamental Mechanisms to Milling Behaviour, Bioengineering, 2018, **5**(2), 41.

4 B. Piriou, G. Vaitilingom, X. Rouau, Solid Fuel in the Form of a Powder, Including a Lignocellulosic Component, WO2013108177A1, France, 2013.

5 T. Abbasi and S. A. Abbasi, Dust explosions–Cases, causes, consequences, and control, J. Hazard. Mater., 2007, **140**(1), 7–44.

6 L. Stover, et al., A phenomenological description of biomass powder combustion in internal combustion engines, Energy, 2023, **274**, 127287.

7 L. Stover, et al., The Biomass Dust-Fueled Engine, in 26th European Biomass Conference & Exhibition, Copenhagen, 2018.

8 B. Piriou, et al., Potential direct use of solid biomass in internal combustion engines, Prog. Energy Combust. Sci., 2013, **39**(1), 169–188.

9 N. Blanc, et al., Breakage of Flawed Particles by Peridynamic Simulations, Comput. Part. Mech., 2021, **8**, 1019–1031.

10 J. Cai, et al., Review of physicochemical properties and analytical characterization of lignocellulosic biomass, Renewable and Sustainable Energy Reviews, 2017, **76**, 309–322.

11 G. G. D. Silva and S. G. X. Rouau, Successive centrifugal grinding and sieving of wheat straw, Powder Technol., 2011, **208**(2), 266–270.

12 C. Gao, et al., Regularity and mechanism of wheat straw properties change in ball milling process at cellular scale, Bioresour. Technol., 2017, **241**, 214–219.

13 C. Mayer-Laigle, et al., Properties of Biomass Powders Resulting from the Fine Comminution of Straw and Bark Feedstocks by Three Types of Ball-Mill Set-Up (RBM, SBM, VBM), Portail Data INRAE, 2021.

14 K. R. Rajaonarivony, et al., Comparative comminution efficiencies of rotary, stirred and vibrating ball-mills for the production of ultrafine biomass powders, Energy, 2021, **227**, 120508.

15 G. G. D. Silva, et al., Effects of grinding processes on enzymatic degradation of wheat straw, Bioresour. Technol., 2012, **103**(1), 192–200.

16 R. Rajaonarivony, et al., Properties of biomass powders resulting from the fine comminution of lignocellulosic feedstocks by three types of ball-mill set-up [version 2; peer review: 2 approved], Open Research Europe, 2022, **1**(125).

17 M. J. Prins, K. J. Ptasinski and F. J. J. G. Janssen, More efficient biomass gasification via torrefaction, Energy, 2006, **31**(15), 3458–3470.

18 M. J. C. van der Stelt, et al., Biomass upgrading by torrefaction for the production of biofuels: A review, Biomass and Bioenergy, 2011, **35**(9), 3748–3762.

19 D. D. Hu, J. B. Zhuang and M. L. Ding, A Review of Studies on the Granular Agglomeration Mechanisms and Anti-Agglomeration Methods, Key Eng. Mater., 2012, **501**, 515–519.

20 A. Álvarez, et al., Non-oxidative torrefaction of biomass to enhance its fuel properties, Energy, 2018, **158**, 1–8.

21 C. Couhert, S. Salvador and J. M. Commandré, Impact of torrefaction on syngas production from wood, Fuel, 2009, **88**(11), 2286–2290.

22 F. Weiland, et al., Entrained flow gasification of torrefied wood residues, Fuel Process. Technol., 2014, **125**, 51–58.

23 J. Pachón-Morales, et al., Flowability characterization of torrefied biomass powders: Static and dynamic testing, Biomass Bioenergy, 2020, **138**, 105608.

24 J. Pachón-Morales, et al., Effect of torrefaction intensity on the flow properties of lignocellulosic biomass powders, Biomass Bioenergy, 2019, **120**, 301–312.

25 B. Etia-group and S. A. S. Etia, Thermal Processing of Powders: Introducing the Spirajoule, Heating Screw Conveyor Powered by Electricity, 2019.

26 A. Leroy, et al., Evaluating polymer interplay after hot water pretreatment to investigate maize stem internode recalcitrance, Biotechnol. Biofuels, 2021, **14**(1), 164.

27 M. Bardet, et al., Dynamics property recovery of archaeological-wood fibers treated with polyethylene glycol demonstrated by high-resolution solid-state NMR, Cellulose, 2012, **19**(5), 1537–1545.

28 P. T. Larsson, K. Wickholm and T. Iversen, A CP/MAS13C NMR investigation of molecular ordering in celluloses, Carbohydr. Res., 1997, **302**(1), 19–25.

29 M. Lahaye, et al., Cellulose, pectin and water in cell walls determine apple flesh viscoelastic mechanical properties, Carbohydr. Polym., 2020, **232**, 115768.

30 R. Hatfield and R. S. Fukushima, Can Lignin Be Accurately Measured?, Crop Science, 2005, **45**(3), 832–839.

31 Sader, Available from: https://sadermethod.org/.

32 Gwyddion, Available from: http://gwyddion.net.

33 Afnor, Biocombustibles solides - Méthode pour la détermination du pouvoir calorifique, 2005, p. 66.

34 G. B. J. de Boer, et al., Laser Diffraction Spectrometry: Fraunhofer Diffraction Versus Mie Scattering, Part. Part. Syst. Charact., 1987, **4**(1-4), 14–19.

35 K. Rajaonarivony, et al., Fine Comminution of Pine Bark: How Does Mechanical Loading Influence Particles Properties and Milling Efficiency?, Bioengineering, 2019, **6**(4), 102.

36 R. Freeman, Measuring the flow properties of consolidated, conditioned and aerated powders — A comparative study using a powder rheometer and a rotational shear cell, Powder Technol., 2007, **174**(1), 25–33.

37 A. Alonso-Simón, et al., High-throughput microarray profiling of cell wall polymers during hydrothermal pre-treatment of wheat straw, Biotechnol. Bioeng., 2010, **105**(3), 509–514.

38 A. Villares, *et al.*, Lytic polysaccharide monooxygenases disrupt the cellulose fibers structure, *Sci. Rep.*, 2017, **7**(1), 40262.

39 J.-L. Wen, *et al.*, Understanding the chemical and structural transformations of lignin macromolecule during torrefaction, *Appl. Energy*, 2014, **121**, 1–9.

40 M. Eder, *et al.*, Experimental micromechanical characterisation of wood cell walls, *Wood Sci. Technol.*, 2013, **47**(1), 163–182.

41 D. Siniscalco, *et al.*, Monitoring temperature effects on flax cell-wall mechanical properties within a composite material using AFM, *Polym. Test.*, 2018, **69**, 91–99.

42 A. Melelli, *et al.*, The Middle Lamella of Plant Fibers Used as Composite Reinforcement: Investigation by Atomic Force Microscopy, *Molecules*, 2020, **25**, DOI: **10.3390/molecules25030632**.

43 P. Rittinger, *Lehrbuch Der Aufbereitungskunde in Ihrer Neuesten Entwicklung Und Ausbildung Systematisch Dargestellt*, Ernst & Sohn, Berlin, Germany, 1867.

44 N. Blanc, *et al.*, Evolution of grinding energy and particle size during dry ball-milling of silica sand, *Powder Technol.*, 2020, **376**, 661–667.

45 L. Opoczky, Fine grinding and agglomeration of silicates, *Powder Technol.*, 1977, **17**(1), 1–7.

46 M. Almendros, *et al.*, Changes on wood powder morphology and flowability due to thermal pretreatment, in *Récents Progrès en Génie des Procédés*, SFGP, Paris, France, 2011.

47 R. L. Carr, Evaluating Flow Properties of Solids, *Chem. Eng.*, 1965, **72**, 69.

48 H. F. Fischmeister and E. Arzt, Densification of Powders by Particle Deformation, *Powder Metall.*, 1983, **26**(2), 82–88.

49 R. M. Rowell, *Handbook of Wood Chemistry and Wood Composites*, Taylor & Francis, 2nd edn, 2012.

50 M. C. Jarvis, Hydrogen Bonding and Other Non-covalent Interactions at the Surfaces of Cellulose Microfibrils, *Cellulose*, 2023, **30**, 667–687.

51 R. L. Silveira, *et al.*, Plant Biomass Recalcitrance: Effect of Hemicellulose Composition on Nanoscale Forces that Control Cell Wall Strength, *J. Am. Chem. Soc.*, 2013, **135**(51), 19048–19051.

52 J. C. Mortimer, *et al.*, Absence of branches from xylan in Arabidopsis gux mutants reveals potential for simplification of lignocellulosic biomass, *Proceedings of the National Academy of Sciences*, 2010, **107**(40), 17409–17414.

53 P. Basu, Chapter 4 - Torrefaction, in *Biomass Gasification, Pyrolysis and Torrefaction*, ed. P. Basu, Academic Press, Boston, 2nd edn, 2013, pp. 87–145.

54 R. Bass, *et al.*, Carbon Implications of Converting a Coal-Fired Power Plant to Combustion of Torrefied Arundo Donax, *Applied Bioenergy*, 2014, **1**.

55 L. J. R. Nunes, J. C. De Oliveira Matias, and J. P. Da Silva Catalão, Chapter 3 - Biomass Torrefaction Process, in *Torrefaction of Biomass for Energy Applications*, ed. L. J. R. Nunes, J. C. de Oliveira Matias, and J. P. Da Silva Catalão, Academic Press, 2018, pp. 89–124.

56 B. Colin, *Modelling of Wood Chips Torrefaction in a Rotary Kiln and Experimental Validation in a Continuous Pilot-Scale Rotary Kiln*, Ecole des Mines d'Albi-Carmaux, 2014.